



Cite this: *Mater. Adv.*, 2022, 3, 362

Received 10th August 2021,  
Accepted 1st November 2021

DOI: 10.1039/d1ma00708d

rsc.li/materials-advances

## Polymer-templated mesoporous lithium titanate microspheres for high-performance lithium batteries†

Minh Tri Nguyen, <sup>a</sup> Preston Sutton, <sup>‡ab</sup> Andrea Palumbo, <sup>a</sup> Michael G. Fischer, <sup>§a</sup> Xiao Hua, <sup>c</sup> Ilja Gunkel <sup>\*a</sup> and Ullrich Steiner <sup>\*a</sup>

The spinel  $\text{Li}_4\text{Ti}_5\text{O}_{12}$  (LTO) is a promising lithium ion battery anode material with the potential to supplement graphite as an industry standard, but its low electrical conductivity and Li-ion diffusivity need to be overcome. Here, mesoporous LTO microspheres with carbon-coatings were formed by phase separation of a homopolymer from microphase-separated block copolymers of varying molar masses containing sol–gel precursors. Upon heating the composite underwent a sol–gel condensation reaction followed by the eventual pyrolysis of the polymer templates. The optimised mesoporous LTO microspheres demonstrated an excellent electrochemical performance with an excellent specific discharge capacity of  $164 \text{ mA h g}^{-1}$ , 95% of which was retained after 1000 cycles at a C-rate of 10.

## 1 Introduction

The continued growth of lithium-ion batteries (LIBs) for transportation and power applications requires cell-level performance improvements.<sup>1</sup> While these improvements can be realised by optimising all battery components,<sup>2</sup> the anode is the principal focus of this paper. Graphite is currently the most widely used commercial anode material, although its low rate performance, safety concerns related to lithium dendrite growth, and material degradation are slowing battery development for vehicles and high power systems.<sup>3,4</sup> A promising alternative to graphite and its limitations is lithium titanate,  $\text{Li}_4\text{Ti}_5\text{O}_{12}$  (LTO).<sup>5–7</sup>

LTO has proven to be a safe, low-cost, and electrochemically stable anode material with excellent thermal stability and increased cyclability compared to graphite.<sup>8,9</sup> An important advantage of LTO is its flat (de)lithiation potential well above the voltage of lithium plating (0 V vs.  $\text{Li}^+/\text{Li}$ ), preventing the fire and explosion risks caused by dendrite formation in graphite cells. In addition, the stable LTO spinel structure ( $Fd\bar{3}m$  space group) exhibits negligible volume change during (de)lithiation,

which enables fast (dis)charging.<sup>4,9</sup> This is in contrast to graphite, which expands up to 13% by volume during lithiation,<sup>10</sup> causing a host of degradation issues. While the high redox potential of LTO with respect to lithium reduces the voltage of any cell, and thus its energy density ( $175 \text{ mA h g}^{-1}$  discharged to 1.0 V vs.  $\text{Li}^+/\text{Li}$ , compared to  $372 \text{ mA h g}^{-1}$  discharged to almost 0 V vs.  $\text{Li}^+/\text{Li}$ , for graphite),<sup>8,11</sup> the high potential inhibits the decomposition of contemporary carbonate-based electrolytes, extending the useful cycle life well beyond that of graphite-based cells.<sup>2</sup>

However, to fully realise the benefits of LTO over graphite, its intrinsically low electrical conductivity (*ca.*  $10^{-8}$  to  $10^{-13} \text{ S cm}^{-1}$ ) and its low lithium-ion diffusion coefficient ( $10^{-8}$  to  $10^{-13} \text{ cm}^2 \text{ s}^{-1}$ )<sup>12</sup> must be addressed. These underlying rate-limiting properties of LTO can be improved through several strategies, including surface coatings, doping, or control of particle size and morphology, which determine the effective reaction area and Li-ion diffusion lengths.<sup>11–14</sup> Nanostructuring, for example, generally reduces diffusion paths and increases surface area, which allows for higher (dis)charging rates by increasing the number of reaction sites. A mere size reduction of the traditionally micrometer-sized LTO particles to the nanoscale causes however also a low volumetric energy density and poor particle–particle interconnections.<sup>11</sup> These drawbacks of LTO nanoparticles can be circumvented by introducing nanometer-sized pores into micrometer-sized particles. Such hierarchical structures, which are referred to as mesoporous microspheres combine short lithium-ion diffusion paths and high surface areas with a high volumetric energy density and structural stability.<sup>11,12</sup>

<sup>a</sup> Adolphe Merkle Institute, University of Fribourg, Chemin des Verdiers 4, 1700 Fribourg, Switzerland. E-mail: [ilja.gunkel@unifr.ch](mailto:ilja.gunkel@unifr.ch), [ullrich.steiner@unifr.ch](mailto:ullrich.steiner@unifr.ch)

<sup>b</sup> Institute for Frontier Materials, Deakin University, Burwood, VIC 3125, Australia

<sup>c</sup> Department of Chemical and Biological Engineering, University of Sheffield, UK

† Electronic supplementary information (ESI) available. See DOI: [10.1039/d1ma00708d](https://doi.org/10.1039/d1ma00708d)

‡ Present address: BeDimensional S. p. A., Via Lungo Torrente Secca 30R, 16163 Genova, Italia

§ Present address: Sensirion AG, Laubisruetistrasse 50, 8712 Staefa ZH, Switzerland.



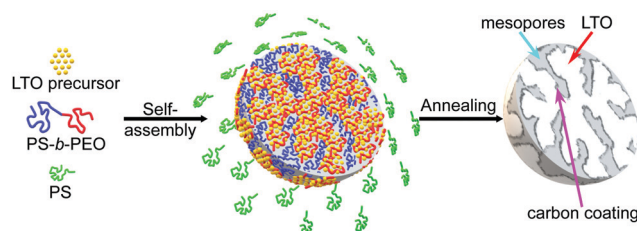


**Fig. 1** Schematic of the polymer-templated fabrication of carbon-coated mesoporous LTO microspheres. Initially, LTO precursors, PS-*b*-PEO block copolymers (BCPs) and PS homopolymer are mixed in a common solvent. Upon solvent evaporation, the BCP and the PS homopolymer phase separate into BCP spheres, in which the BCP blocks coassemble into a nanostructured morphology with the LTO precursor molecules preferentially residing in the PEO domains. Annealing this blend in an argon atmosphere causes confined crystallisation of the LTO while the polymer template is burnt away and partially carbonised, thereby creating LTO microspheres with carbon-coated mesopores.<sup>15,17,18,22,23</sup>

Mesoporous LTO microspheres can be prepared using various synthetic approaches, including hydrothermal<sup>15,16</sup> and solvothermal methods,<sup>17,18</sup> which both improve the rate performance. For example, Tang *et al.* used a hydrothermal process to prepare mesoporous LTO spheres that showed excellent high-rate capabilities with a specific capacity of 114 mA h g<sup>-1</sup> at 30 °C as well as good cycle performance with a 94.5% capacity retention after 200 cycles at 4 °C.<sup>15</sup> To further improve the rate performance of these hierarchically structured materials, fine control over particle and pore size is desirable. In this regard, the use of polymer templates provides a powerful tool. In an earlier study, we have shown the efficacy of combining block copolymer (BCP) self-assembly and polymer phase separation with a sol-gel chemistry for precise structure templating in TiO<sub>2</sub> microspheres, *i.e.* in a similar material to the LTO studied here.<sup>19</sup> BCP self-assembly was also previously used to introduce mesoporosity into LTO.<sup>20</sup>

Here, we extend the facile one-pot synthesis approach using polymer templates to the fabrication of mesoporous LTO microspheres with tunable mesopore sizes. The desired micron-sized spherical particles were produced *via* polymer phase separation, while co-assembly of LTO sol-gel precursors with amphiphilic BCPs created a mesoporous structure upon sol-gel condensation during high-temperature annealing in argon. This annealing process forms a very thin graphitic layer on the mesoporous surface of the LTO microspheres, substantially increasing the intrinsically low electric conductivity of LTO.<sup>21</sup>

The mesoporosity of the microspheres was adjusted by varying the BCP molar mass, enabling the optimization of the LTO rate performance. The resulting polymer-templated anode material showed excellent properties, achieving 113 mA h g<sup>-1</sup> at 30 °C with a capacity retention of 95% after 1000 cycles at 10 °C, demonstrating superior cyclability compared to earlier studies.<sup>15,17,18,22,23</sup>

## 2 Results and discussion

### 2.1 Fabrication of mesoporous Li<sub>4</sub>Ti<sub>5</sub>O<sub>12</sub> (LTO) microspheres

Mesoporous LTO microspheres were prepared by confining their sol-gel synthesis in hierarchical polymer templates, in a two-step fabrication process consisting of the coassembly of a sol precursor with a suitable BCP followed by a temperature-induced condensation reaction and calcination to carbon-coated LTO, Fig. 1. The amphiphilic poly(styrene-*b*-ethylene oxide) (PS-*b*-PEO) BCPs enable the selective complexation of LTO precursor alkoxides with the hydrophilic PEO block.<sup>20,24</sup> The self-assembly of this complex (*i.e.* the microphase separation of the hydrophilic PEO-complex and the hydrophobic PS block) causes the formation of a nanostructure in solution.<sup>25</sup> The addition of a PS homopolymer to this blend causes the mixture to further phase separate at a different length scale, giving rise to micrometer-sized spheres of the LTO-BCP coassembly. Nanostructured microspheres are thus formed in a one-pot synthesis by mixing the polymers and the LTO precursors in a common solvent (tetrahydrofuran (THF)), plus oxalic acid to stabilise the sol-gel process,<sup>19</sup> followed by slow solvent evaporation. The resulting mesoporous LTO microspheres are calcined at 600 °C or 700 °C in argon, causing the confined crystallisation of LTO inside the polymer template. The organic matrix is gradually pyrolysed and partially carbonised at these temperatures, resulting in LTO microparticles with carbon-coated nanopores.<sup>21</sup> This approach allows tuning of the pores sizes, as previously demonstrated for mesoporous TiO<sub>2</sub> microspheres.<sup>19</sup>

To adjust the size of the mesopores,<sup>19</sup> PS-*b*-PEO BCPs with different molar masses but similar block volume fractions were used. The molar mass of the added PS homopolymer was either higher or similar to that of the PS blocks in the PS-*b*-PEO BCPs to ensure phase separation and microparticle formation. The different mesoporous LTO microsphere samples synthesised in

**Table 1** Sample names and descriptions. The sample names specify the employed BCP (BCP name) and the calcination temperature. Columns 4–8 list the BCP molar mass ( $M_n$ ) and composition, the PS weight fraction ( $w_{PS}$ ) of the BCP,  $M_n$  of the PS homopolymer, and the calcination temperature and time, respectively

LTO name	BCP name	BCP	$M_n$ (kg mol <sup>-1</sup> )	$w_{PS}$	$M_n$ (kg mol <sup>-1</sup> )	Calcination	
						T (°C)	Time (h)
LTO-A-600	BCP <sub>A</sub>	PS- <i>b</i> -PEO	10- <i>b</i> -3.5	~0.74	35	600	2.5
LTO-A-700	BCP <sub>A</sub>	PS- <i>b</i> -PEO	10- <i>b</i> -3.5	~0.74	35	700	2.5
LTO-B-600	BCP <sub>B</sub>	PS- <i>b</i> -PEO	18- <i>b</i> -7.5	~0.71	35	600	2.5
LTO-B-700	BCP <sub>B</sub>	PS- <i>b</i> -PEO	18- <i>b</i> -7.5	~0.71	35	700	2.5
LTO-C-700	BCP <sub>C</sub>	PS- <i>b</i> -PEO	38- <i>b</i> -15	~0.72	35	700	2.5



this work were named based on the employed BCPs and the calcination temperatures, Table 1.

## 2.2 Phase structure and morphology of mesoporous LTO microspheres

**2.2.1 Phase structure.** The crystalline structures of all synthesised LTO samples were characterised by X-ray diffraction (XRD), Fig. 2. Indexing of the XRD patterns confirms a

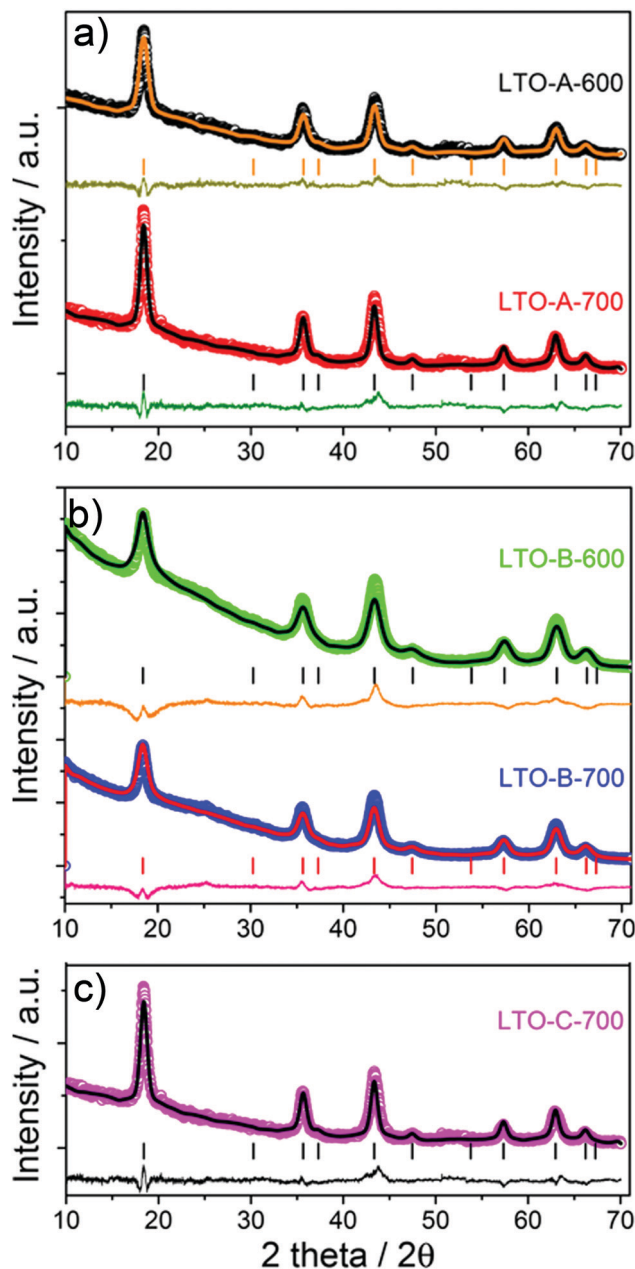


Fig. 2 XRD patterns of the mesoporous LTO microspheres listed in Tables 1 and 2, (a) LTO-A, (b) LTO-B and (c) LTO-C. The symbols show the experimental data and the lines are fitted Rietveld refinements. The vertical bars indicate the tabulated peak positions for spinel LTO, below which the differences between experimental data and fits are plotted. In (c) the peaks expected for a spinel structure (space group:  $Fd\bar{3}m$ ) are indexed with the  $(hkl)$  values of the corresponding lattice planes.

spinel structure (COD card no. 99-100-1099, space group:  $Fd\bar{3}m$ ) for all  $Li_4Ti_5O_{12}$  samples, as well as the absence of any discernible impurity phases such as anatase or rutile. The XRD patterns show a decreasing peak width, and thus an increasing crystallite size with increasing calcination temperature. The average crystallite sizes in Table 2 were calculated using the Scherrer equation ( $K = 0.9$ ) by averaging the values obtained for the (111), (131), (040), (151), and (404) planes.<sup>26</sup>

This careful analysis of crystallite sizes shows two interesting trends. First, the crystallite size increases with increasing calcination temperatures, as expected. Note that this increase is more pronounced in LTO-A compared to LTO-B. A moderate increase in crystallite size with calcination temperature reflects temperature-dependent crystallisation kinetics, which explain the small crystallite-size increase in LTO-B-700 compared to LTO-B-600. Second, the crystallite size is larger in LTO-A than in LTO-B, despite the fact that the lower molar mass of BCP<sub>A</sub> should yield a tighter LTO confinement than LTO-B. Indeed, LTO-A crystallite sizes are comparable to or larger than those of LTO-C, despite the 4-fold larger molar mass of the confining BCP<sub>C</sub> template. These observations are indicative of a less effective confinement of LTO crystallisation provided by the low-molar mass BCP<sub>A</sub> template compared to the other two BCPs, which is likely due to a weaker segregation in BCPs with shorter blocks. This hypothesis is further substantiated by the nitrogen physisorption experiments described below.

The spinel structure of all mesoporous LTO microspheres was further confirmed by Raman spectroscopy, Fig. 3. The spinel LTO has five first-order Raman modes, namely,  $1 \times A_{1g}$ ,  $1 \times E_g$ ,  $3 \times F_{2g}$ , according to group theory.<sup>27,28</sup> These bands were observed at around  $230\text{ cm}^{-1}$  ( $F_{2g}$ ),  $404\text{ cm}^{-1}$  ( $E_g$ ) and  $675\text{ cm}^{-1}$  ( $A_{1g}$ ) along with a shoulder at about  $750\text{ cm}^{-1}$ , for all LTO samples, which is in good agreement with spinel LTO,<sup>29–31</sup> and corroborates the XRD results. The band at  $230\text{ cm}^{-1}$  is assigned to the bending vibration of the O–Ti–O bonds.<sup>30</sup> The band at  $404\text{ cm}^{-1}$  is attributed to the stretching vibration of the Li–O bonds in tetrahedral  $LiO_4$  and polyhedral  $LiO_6$ .<sup>27,30</sup> The bands at  $675$  and  $750\text{ cm}^{-1}$  ( $A_{1g}$ ) correspond to the vibration of the Ti–O bonds in octahedral  $TiO_6$ .<sup>28,31</sup> Furthermore, two weak bands at around  $1340\text{ cm}^{-1}$  and  $1600\text{ cm}^{-1}$  corresponding to the D band and the G band of carbon, respectively, confirm the presence of carbon resulting from pyrolysis of the polymers upon the annealing at high temperature.<sup>32,33</sup> While the D and G bands are clearly seen in the spectra of the LTO-A-600 and LTO-B-600 samples, their intensity is lower in the LTO-A-700 and LTO-B-700 spectra indicating a lower carbon content in samples calcined at the higher temperature. The peak area ratios  $A_D/A_G$  of about 1.33 for LTO-A-600, 1.23 for LTO-A-700, 1.28 for LTO-B-600, 1.25 for LTO-B-700, and 1.53 for LTO-C-700, imply predominantly disordered (amorphous) carbon layers in all samples.<sup>34</sup>

While XRD and Raman measurements reveal no impurities in any LTO samples, lithium carbonate and hydroxy groups are seen in the FTIR spectra, Fig. S1 (ESI<sup>†</sup>). The presence of  $Li_2CO_3$  in the synthesised LTO samples probably arises from the reaction of lithium ions with  $CO_2$  at the sample surface, while



**Table 2** Summary of the average crystallite sizes from XRD analysis, surface areas  $S_{\text{BET}}$  and pore volumes  $V_{\text{pore}}$  based on BET analysis from the adsorption branch, specific capacities from the galvanostatic analysis, Coulombic efficiency (CE) from the first cycle at a C-rate of 0.5, specific capacities after 5 cycles and after 1000 cycles at a C-rate of 10 from cycle testing; Potential difference ( $\Delta E$ ) from the CV measurements at a scan rate of  $0.1 \text{ mV s}^{-1}$ , post-assembly (a), post-rate test (b), and post-cycle test (c); impedance values as determined from the EIS measurements, post-assembly (a), post-cycle test (c). The pore size distribution and the pore volume  $V_{\text{pore}}$  were evaluated by the BJH method from the adsorption branch; Specific discharge capacity of the 1<sup>st</sup> cycles at a C-rate of 0.5, and the 10 cycles at a C-rate of 0.5, 10 and 30

Sample	Crystallite-size (nm)	$S_{\text{BET}}$ ( $\text{m}^2 \text{ g}^{-1}$ )	$V_{\text{pore}}$ ( $\text{cm}^3 \text{ g}^{-1}$ )	Rate test ( $\text{mA h g}^{-1}$ )				CE (%)	Cycle test ( $\text{mA h g}^{-1}$ )			$\Delta E$ (V)	Total resistances ( $\Omega$ )			
				0.5 C		10 C			30 C		0.5 C		10 C			
				1 <sup>st</sup>	10 <sup>th</sup>	10 <sup>th</sup>	10 <sup>th</sup>		1 <sup>st</sup>	10 <sup>th</sup>	1 <sup>st</sup>	10 <sup>th</sup>	1 <sup>st</sup>	10 <sup>th</sup>		
LTO-A-600	10.02	75.6	0.133	156	143	113	93	94.7	108	96	0.26	0.09	0.09	210	58	
LTO-A-700	12.17	54.4	0.122	156	139	107	85	92.3	99	86	0.28	0.10	0.11	144	51	
LTO-B-600	8.42	123.3	0.168	161	143	104	54	92.2	101	97	0.16	0.09	0.07	263	100	
LTO-B-700	9.78	110.6	0.162	164	147	127	113	91.9	128	122	0.22	0.09	0.09	159	48	
LTO-C-700	10.90	68.3	0.078	88	72	28	16	91.9	26	24	0.15	0.09	0.11	140	133	

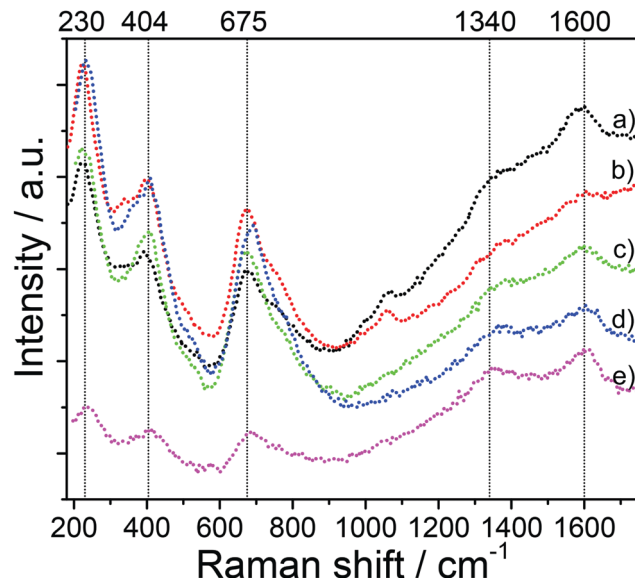


**Fig. 3** Raman spectra of the mesoporous LTO microspheres. (a) LTO-A-600, (b) LTO-A-700, (c) LTO-B-600, (d) LTO-B-700, and (e) LTO-C-700.

the presence of OH groups is associated with adsorbed  $\text{H}_2\text{O}$  from ambient air.<sup>35</sup> Small amounts of (disordered) carbon ( $\leq 6$  wt%) and water ( $\leq 3$  wt%) in the synthesised LTO were found also in thermogravimetric analysis (TGA), Fig. S1 (ESI<sup>†</sup>). Similar amounts of carbon were detected in mesoporous  $\text{TiO}_2$  microspheres that were coated with a 1.0 to 1.5 nm thick carbon layer as seen in high-resolution TEM imaging (Fig. S11 (ESI<sup>†</sup>), M.G. Fischer *et al.*).<sup>19</sup>

**2.2.2 Morphology.** The structure and morphology of the mesoporous LTO material was imaged by scanning electron microscopy (SEM), Fig. 4. The low-magnification images in the middle column show LTO spheres with diameters in the 1–10  $\mu\text{m}$  range. The higher-magnification images in the right column of Fig. 4 show the mesoporous nanomorphology of these spheres. Zooming out further (middle and left columns)

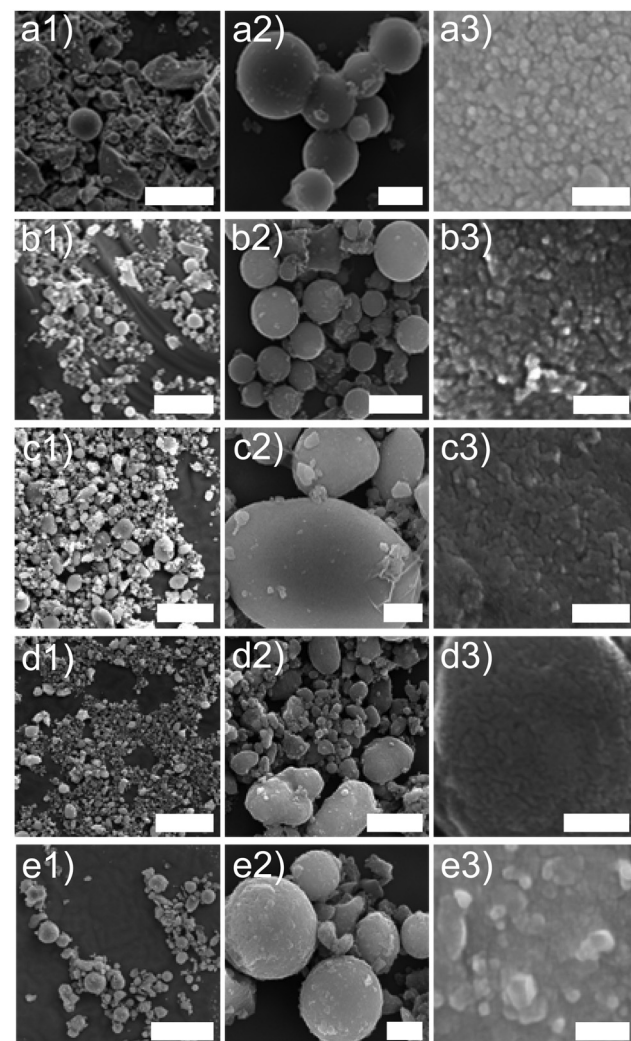
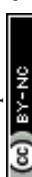


**Fig. 4** Low to high magnification SEM images (left to right columns) of mesoporous LTO-A-600 (a), LTO-A-700 (b), LTO-B-600 (c), LTO-B-700 (d), and LTO-C-700 (e) showing the predominance of LTO spheres exhibiting mesoporosity. Left column scale bar: 20  $\mu\text{m}$ , centre column scale bar: 2  $\mu\text{m}$ , right column scale bar: 100 nm.



shows rather polydisperse particle sizes on the one hand, and the presence of non-spherical material on the other hand, particularly in Fig. 4d. The latter observation, coupled with XRD and Raman results showing the formation of pure LTO, leads to two possible hypotheses related to the origin of the non-spherical material. Either it results from a non-confined LTO synthesis (*i.e.* precursor that did not complex with the BCP), or it arises from severe break-out crystallisation which completely destroyed the polymer-induced morphology. The presence of BCP-induced mesoporosity, even in the irregular, non-spherical morphologies seen in the higher magnification images of Fig. 4, seems to favour break-out crystallisation as the culprit since non-complexed LTO should have no such structure.

The pore size, volume, and surface area of the five LTO sample types were quantified by measuring nitrogen physisorption isotherms, which were analysed by the Brunauer–Emmett–Teller (BET) formalism, Fig. 5a. All LTO samples show type-IV isotherms, which are typical for mesoporous materials.<sup>36</sup> Their different hysteresis loops imply differences in their pore structures. The type-H1 hysteresis loop observed for the LTO-A-600, LTO-A-700, LTO-B-600 and LTO-B-700 samples is indicative of highly uniform pore sizes, high pore connectivities, and cylindrical pore geometries. In contrast, the type-H4 hysteresis loop of the LTO-C-700 sample suggests the presence of some large mesopores in addition to a large fraction of much smaller pores.<sup>36,37</sup> Note the decrease in porosity with increasing annealing temperatures, which correlates with the increased crystallite sizes.<sup>19</sup>

The Barrett–Joyner–Halenda (BJH) analysis in Fig. 5b and in Fig. S7 (ESI<sup>†</sup>) was used to determine the pore-size distribution of the samples, revealing bimodal pore size distributions. The larger-sized pores are assigned to the polymer templating, while the smaller sized pores are intrinsic to the sol–gel chemistry, which is known to give rise to nanopores even in the absence of any macromolecular additives.<sup>38</sup> The smaller, *ca.* 2 nm pores are similar in all samples, while the larger pores vary from  $\sim 5$  nm to  $\sim 20$  nm as a function of the chosen BCP and calcination temperature, giving rise to two trends. First, an increase in pore size with increasing BCP molar mass is observed, as expected.<sup>19</sup> Second, an interesting aspect arises

from the comparison of BET and BJH isotherms of the two LTO-A and the two LTO-B samples. Note that the  $\sim 7$  nm LTO-B pore size is invariant with the calcination temperature, while the 4.6 nm pores size of LTO-A-600 increases to 5.7 nm in LTO-A-700. The BET pore volumes of the LTO-A samples (see Table 2) are much lower compared to the LTO-B samples, despite the expectation that the lower-molar mass BCP should give rise to a higher porosity. Furthermore, the pore volume of LTO-A-700 is reduced compared to LTO-A-600, while the two LTO-B samples have identical pore volumes.

Combining these observations with the Scherrer analysis of the XRD data in Fig. 2 leads to conclusions concerning the structure formation in LTO-A and LTO-B. The invariance of porosity in LTO-B with the calcination temperature indicates that the LTO morphology is robustly templated by the BCP. The pore volume is stable at the two calcination temperatures and the crystallite and pore diameters are comparable. In LTO-A, however, the pore volume is comparably lower and decreases further with the calcination temperature, indicating structural degradation and the formation of fewer larger pores. The crystallite sizes are not only larger in LTO-A, they are substantially larger than the LTO-B crystallite sizes, and both increase with increasing calcination temperature. These observations are indicative of break-out crystallisation, where the crystallisation process of LTO partially destroys the confining polymeric template.

Finally, the LTO-C sample has a low porosity caused by the high molar mass of BCP-C, resulting in an inferior material in terms of mesoporosity compared to LTO-B, as qualitatively expected.

### 2.3 Electrochemical performance of mesoporous LTO microspheres

In order to optimise electrochemical performance, mesoporous LTO microsphere composite electrodes with different porosities, surface areas, and crystallite sizes were tested. The lithium-ion storage properties of these samples were analysed under galvanostatic conditions in Swagelok cells at various C-rates (a C-rate of 1 equals a current of  $175 \text{ mA g}^{-1}$ ) with a voltage range of 1.0 to 2.5 V *vs.*  $\text{Li}^+/\text{Li}$ , using Li metal as counter electrode.

To determine the initial specific capacities and the Coulombic efficiencies of the samples, the galvanostatic discharge and charge profiles of the first four cycles were measured at a C-rate of 0.5, Fig. 6. The initial specific discharge capacities for LTO-A-600, LTO-A-700, LTO-B-600, LTO-B-700, and LTO-C-700 were found to be 156, 156, 161, 164, and  $88 \text{ mA h g}^{-1}$ , Table 2. LTO-B samples showed the highest specific capacities, correlating with the highest specific surface area of the samples. The slightly higher specific capacity of LTO-B-700 compared to LTO-B-600 might arise from the larger LTO crystallite size and potentially an overall higher crystallinity.<sup>39–41</sup>

The relatively low capacity of LTO-C-700 probably arises from the low porosity of this material, *i.e.* its low pore volume and low specific surface area, (Fig. 5b and Table S1, ESI<sup>†</sup>). While the initial capacities of the LTO-B and LTO-A samples are lower than the theoretical capacity value of  $175 \text{ mA h g}^{-1}$ , they

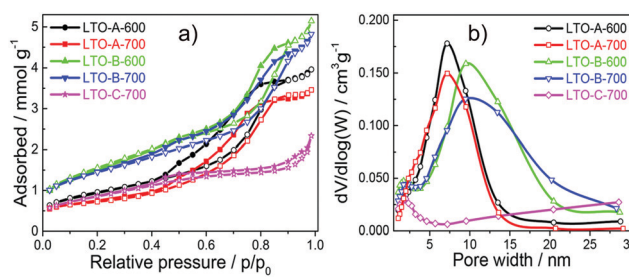


Fig. 5 (a) Nitrogen physisorption isotherms of the mesoporous LTO microspheres at 77 K. (b) Pore size distribution as determined from the adsorption branch using the BJH method, where the derivative pore volume normalised to the natural logarithm of pore-width interval,  $dV/d \log(W)$ , is shown as a function of the pore width.



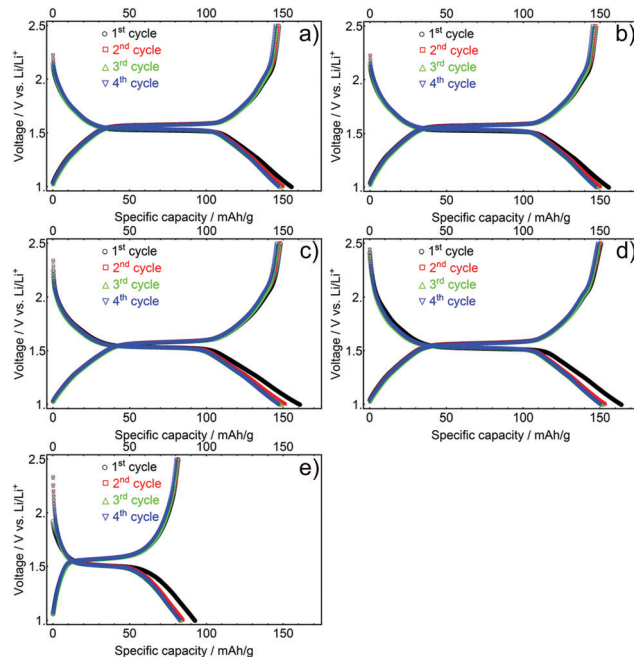


Fig. 6 First four galvanostatic discharge and charge profiles of mesoporous LTO-A-600 (a), LTO-A-700 (b), LTO-B-600 (c), LTO-B-700 (d) and LTO-C-700 (e), C-rate of 0.5.

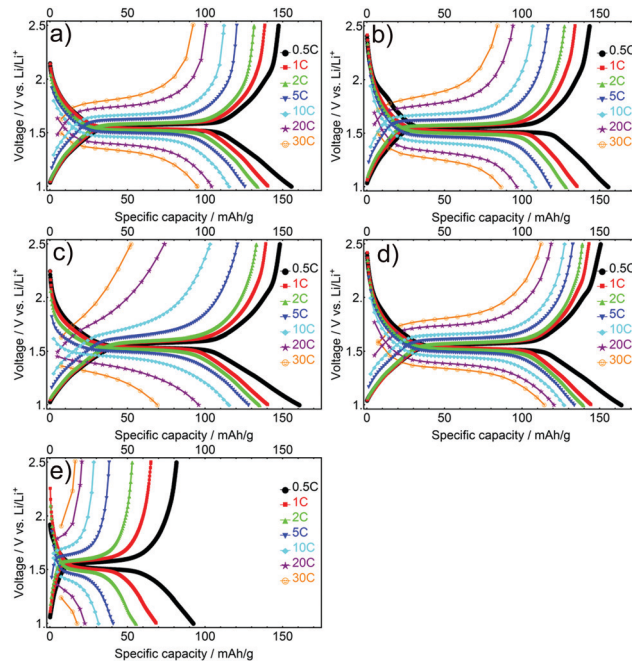


Fig. 7 Initial galvanostatic discharge/charge profiles at different C-rates for the mesoporous LTO-A-600 (a), LTO-A-700 (b), LTO-B-600 (c), LTO-B-700 (d) and LTO-C-700 (e).

are similar if not better than the best-performing state-of-the-art mesoporous LTO materials.<sup>15,17,20,42</sup> Differences between experimental and theoretical capacities during the initial discharge cycles are commonly justified by surface defects, irreversible lithium insertion, and contaminants like residual trace water common to high-surface area materials.<sup>20,41,43,44</sup> It is also possible that the differing pore structures have different electrolyte wettability and interconnectivity, limiting access to electrochemically active material, particularly in LTO-C.

The aforementioned capacity losses during the initial charge-discharge cycle were observed for all samples with Coulombic efficiencies of the initial cycle for the LTO-A-600, LTO-A-700, LTO-B-600, LTO-B-700, and LTO-C-700 being 94.7, 92.3, 92.2, 91.9, and 91.9%, respectively. The efficiency increased upon further cycling, with a value above 97% in the second cycle for all samples. Furthermore, charge/discharge plateau potentials in between 1.5 and 1.6 V were observed for all LTO samples. These plateaus correspond to the topotactic transformation of spinel  $\text{Li}_4\text{Ti}_5\text{O}_{12}$  into rock salt type  $\text{Li}_7\text{Ti}_5\text{O}_{12}$ , with the exact voltage also affected by the crystallite size of the sample.<sup>8,27</sup> The discharge potentials decreased with increasing crystallite size, resulting from a higher calcination temperature, *i.e.* 1.54 V compared to 1.52 V for calcination at 600 °C (*e.g.* LTO-A-600 and LTO-B-600) *vs.* 700 °C (*e.g.* LTO-A-700, LTO-B-700, and LTO-C-700) Fig. S3 (ESI†).<sup>40,45,46</sup>

The influence of the current density on the electrochemical performance of the mesoporous LTO microsphere samples was analysed by rate testing. The goal was to quantify the effects of morphology factors including different crystallite sizes, specific surface areas and porosity on the rate performance. The initial

charge-discharge profiles for all LTO samples cycled at various C-rates show a decrease in capacity, and an increase in polarization between discharge-charge plateaus as current density is increased, a typical result for rate testing,<sup>12</sup> see Fig. 7. LTO-B-700 exhibited the highest specific charge-discharge capacity at every C-rate, followed by the LTO-A-600, LTO-A-700, LTO-B-600 and LTO-C-700. These results are attributed to an interplay between the pore structure, surface area, and crystallite sizes.<sup>47–49</sup> For example, the crystallite size is known to influence the specific capacity.<sup>40,41,45</sup> This is reflected in the LTO-B-700 and LTO-B-600, samples with relatively similar pore structures (volume and surface area) but different crystallite sizes (LTO-B-700 = 9.78 nm, LTO-B-600 = 8.42 nm). At low C-rates *i.e.*, from 0.5 to 2 C their capacity performance is similar, while it differs greatly at higher C-rates *i.e.*, from 5 to 30 C. At 30 C, the capacity for LTO-B-700 was 113 mA h g<sup>-1</sup> while that of LTO-B-600 was only 54 mA h g<sup>-1</sup>, Table S1 (ESI†). This suggests that the Li host sites in the LTO are somehow restricted by the crystallite boundaries.<sup>41,50</sup> However, the capacity does not directly depend on the crystallite size, as is evident from the comparison of LTO-C, with the two LTO-A samples, which have similar crystallite sizes (which are larger than those of the best performing LTO-B-700 sample), but vastly differing specific capacities. This comparison indicates that the smaller surface area and pore volume of the LTO-C sample is also significant (Table S1, ESI†).

The full performance of LTO samples was investigated by rate tests, 10 cycles at increasing C-rates, followed by a cycle test of 1000 cycles at a C-rate of 10, Fig. 8.

At any given rate, the capacities of all devices were relatively stable except for the initial series at 0.5 C, which reflects the



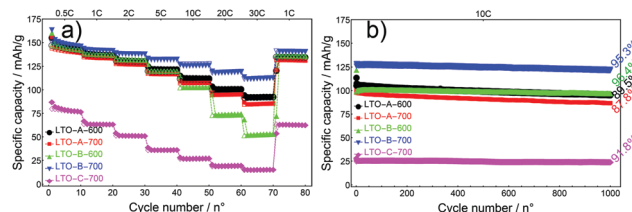


Fig. 8 Rate test (a) and cycle test (b) of mesoporous LTO microsphere composite electrodes. Cycle testing at a C-rate of 10. Percentages indicate capacity retention during cycle testing. The measurements of each sample in (a) and (b) were carried out with the same cells.

conditioning period of the cells. As the current rates increased from a C-rate of 0.5 to 30, the LTO-A-600, LTO-A-700 and LTO-B-700 samples showed very good rate capabilities *i.e.*, their specific capacities decayed from approx. 143, 139, and 147 mA h g<sup>-1</sup> (at a C-rate of 0.5 after 10 cycles) to 93, 85, and 113 mA h g<sup>-1</sup> (at a C-rate of 30 after 10 cycles), respectively, Table 2. Also, their specific capacities mostly recovered upon returning to a C-rate of 1 (Fig. 8a, capacity retention after 75 cycles for LTO-A-600, LTO-A-700, LTO-B-600, LTO-B-700, and LTO-C-700 were 97.9%, 98.2%, 98.4%, 98.8%, and 99.5%, respectively). Note that the rate-dependent capacity of LTO-B-600 in Fig. 8a lies below that which could be expected from most key parameters in Table 2. The much larger-sized particles in Fig. 4c1 and c2 (compared to d1, d2), and their eventual packing in a finished composite electrode might, however, account for the low specific capacities of this material at high C-rates.

The long-term cycling at 10 C for 1000 cycles (post EIS, CV and rate capability tests) showed good stability, Fig. 8b. These results show capacity retention of 89.5% for LTO-A-600, 87.8% for LTO-A-700, 96.4% for LTO-B-600, 95.3% for LTO-B-700, and 91.8% for LTO-C-700 after 1000 cycles with the 5<sup>th</sup> cycle selected as the reference, Table 2. This performance is comparable to previous mesoporous LTO microspheres systems but at a significantly higher cycle number (Table 3), *e.g.*, 94.5% capacity retention after 200 cycles at 4 C by Tang *et al.*,<sup>15</sup> 97.4% capacity retention after 100 cycles at 1 C by Shen *et al.*,<sup>17</sup> 82% capacity retention after 200 cycles at 1 C by Nugroho *et al.*,<sup>22</sup> 86% capacity retention after 100 cycles at 10 C by Lin *et al.*<sup>18</sup>

These results highlight that the detailed LTO morphology including the crystallinity and sample porosity play a pivotal

role in the rate performance and cycling stability. The ability to control these parameters, by employing different annealing temperatures and BCP molar masses, therefore enables the optimisation of the rate capability and cycle stability of LTO material. Specifically, this research suggests that the LTO-B-700 is the most promising candidate for use in LIB electrodes.

Cyclic voltammetry (CV) measurements were taken on each of the LTO samples, using the same cells at 3 different stages, post-assembly, post-rate test, and post-cycle test. The CV results show increasing peak currents  $i_p$  with increasing scan rate  $\nu$ , following the Randles-Ševčík equation, which assumes a diffusion limitation of the active species in the electrode solids,

$$i_p = 0.4463nFAC(nF\nu D/RT)^{1/2}, \quad (1)$$

where  $n$  is number of electrons transferred,  $F$  is Faraday's constant,  $A$  is electrode area,  $C$  is the bulk concentration,  $D$  is the diffusion coefficient,  $R$  is the ideal gas constant, and  $T$  is the temperature (Fig. S4–S6, ESI†). Ideally, the absolute value of the peak ratio between anodic and cathodic current  $i_p$  should be unity and the redox peak potential separation  $\Delta E = E_{p,\text{anodic}} - E_{p,\text{cathodic}}$  should be constant for reversible reactions. Subtle differences in anodic and cathodic peak symmetries of pristine-sample CVs relative to post-cycling CVs are attributed to irreversible reaction products and to different conductivities of the Li<sub>4</sub>Ti<sub>5</sub>O<sub>12</sub> and Li<sub>7</sub>Ti<sub>5</sub>O<sub>12</sub> phases<sup>51,52</sup> caused by the conditioning of the cells. These irreversible products are also seen in the unstable cycling capacity during the first few cycles of the rate test in Fig. 9, and in the change in  $\Delta E$  in all samples at similar scan-rates. The electrochemical polarization  $\Delta E$  is largest after assembly, reducing to consistent values after the rate and cycle tests, Table 2. Further confirmation of the reversible Li-ion

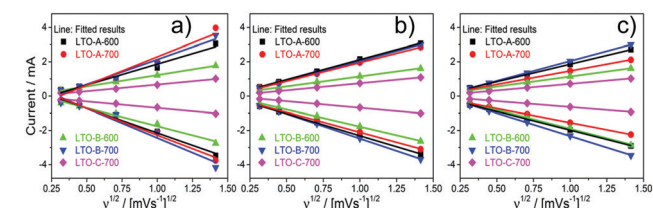


Fig. 9 Peak current  $i_p$  vs. scan rate  $\nu^{1/2}$  of the five mesoporous LTO microsphere samples, (a) post-assembly, (b) post-rate test, and (c) post-cycle test. The slopes in the positive peak current region correspond to the anodic processes, the slopes in the negative peak current region correspond to the cathodic processes.

Table 3 Rate capabilities and cycling performance along with structural characteristics of mesoporous LTO microspheres of the present work\* and previous reports.  $S_{\text{BET}}$ ,  $d_{\text{pore}}$ , and  $V_{\text{pore}}$  denote the surface area, diameter, and volume of the pores, respectively

Sample	Crystallite size (nm)	$S_{\text{BET}}$ (m <sup>2</sup> g <sup>-1</sup> )	$d_{\text{pore}}$ (nm)	$V_{\text{pore}}$ (cm <sup>3</sup> g <sup>-1</sup> )	Specific capacity (mA h g <sup>-1</sup> )				Capacity retention %/number of cycles/C-rate
					1 C	10 C	20 C	30 C	
LTO-B-700*	9.78	110	7.17	0.167	144	126	119	113	95%/1000/10 C
Tang <i>et al.</i> , <sup>15</sup>	n.a.	165.9	9.5	0.46	150	136	n.a.	114	94.5%/200/4 C
Shen <i>et al.</i> , <sup>17</sup>	11	159.4	4.3	0.2	157	140	125	n.a.	97.4%/100/1 C
Nugroho <i>et al.</i> , <sup>22</sup>	32.2	60.2	n.a.	n.a.	159	117	94	61	82%/200/1 C
Lin <i>et al.</i> <sup>18</sup>	n.a.	40.2	4.67	0.077	185	115	n.a.	n.a.	86%/100/10 C



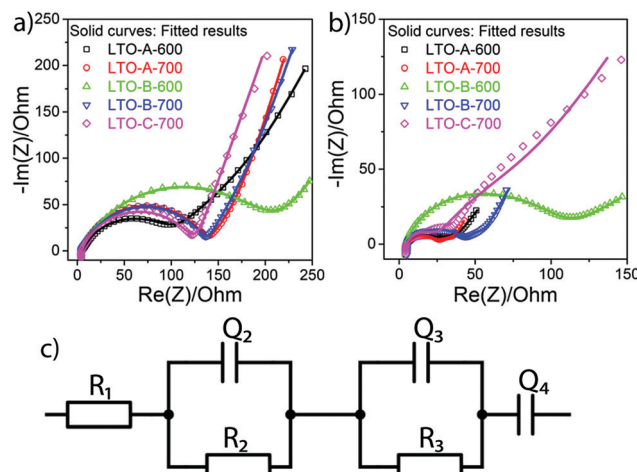


Fig. 10 Nyquist plots of Li-metal/LTO half-cells, before the rate test (a), and after the cycle test (b). The equivalent circuit (c) with  $R_1$  the apparatus resistance and two  $R$ - $Q$  elements, the Li- metal/electrolyte and electrolyte/LTO interfaces.  $Q_4$  accounts for Li-ion diffusion at low frequencies.

insertion into LTO with minimal non-faradaic adsorption is verified by the linear dependence of  $i_p$  vs.  $\nu^{1/2}$  of the Randles-Ševčík equation,<sup>53–55</sup> Fig. 9.

Electrochemical impedance spectroscopy (EIS) was employed to measure the ohmic effects of the mesoporous LTO microsphere morphology. For each sample, EIS measurements were recorded before the rate test and after the cycle test. The EIS spectra of all samples consist of one depressed semi-circle in the high-frequency region and a linear tail in the low-frequency region, Fig. 10. The apparent impedance differences after cycling are attributed to the varying LTO morphologies since the samples are otherwise identical, including the Li-metal counter electrode. Note that all samples show higher total impedance before cycling, Fig. 10, suggesting that there is a conditioning period of the cell in addition to the morphological effects. While the lowering impedance as cycling progresses is consistent with an active material that requires a conditioning period before optimal performance, the Li-metal electrode should also be considered. Even though a solid-electrolyte interface (SEI) does not form on LTO under these conditions, Schweikert *et al.* have identified SEI formation on the Li metal/electrolyte interface in Li/LTO cells as a significant source of initial cell resistance.<sup>56,57</sup> This may also be the source of the impedance variation shown in Fig. 10, where a high initial impedance is lowered through the stable forming of a SEI upon conditioning. Therefore, the EIS spectra of Fig. 10b after conditioning were selected as the accurate reflection of the morphological differences of the LTO samples.

The total resistance values of all LTO samples were calculated based on the equivalent circuit in Fig. 10c, and are summarized in Table 2.  $R_1$ , assigned to the test apparatus including the connections and the Swagelok cell, was approximately  $4.5\ \Omega$  in all measurements, remaining nearly unchanged throughout testing.  $R_2$  and  $R_3$  constitute two distinct  $R$ - $Q$  elements that are related to the charge transfer kinetics at the

two electrolyte interfaces of the electrodes. They vary from  $48$  to  $263\ \Omega$  across samples and tests.  $Q_4$  models the low-frequency Li-ion diffusion in the samples. Post-cycling tests revealed a much lower ohmic resistance of the Li metal/electrolyte interface compared to the other two resistances, so that its  $R$ - $Q$  element can be eliminated in the analysis of the EIS measurements.

It is important to reiterate that an equivalent circuit model is a vast simplification of a complex process. The modelling of the two electrode/electrolyte interfaces in particular are unlikely to perfectly capture the entire scope of all electrochemical and transport processes taking place. However, as the cells are similarly conditioned, post-cycle test EIS should primarily reflect impedance changes caused only by the LTO morphological differences and can therefore be used to effectively compare the different morphological effects on the electrochemical performance.

The total resistances before the rate test ( $\sum R_{\text{bef}} = R_2 + R_3$ ) were  $210\ \Omega$  and  $144\ \Omega$  for LTO-A-600 and LTO-A-700, respectively,  $263\ \Omega$  and  $159\ \Omega$  for LTO-B-600 and LTO-B-700, respectively, and  $140\ \Omega$  for LTO-C-700. The total resistances after the cycle test ( $\sum R_{\text{aft}} = R_2 + R_3$ ) were  $58\ \Omega$  and  $51\ \Omega$  for LTO-A-600 and LTO-A-700, respectively,  $100\ \Omega$  and  $48\ \Omega$  for LTO-B-600 and LTO-B-700, respectively and  $133\ \Omega$  for LTO-C-700. Again, the reduction of the total resistance after the cycling test is associated with a combination of a material conditioning and the formation of a stable SEI layer on the Li-metal electrode.<sup>20,56,57</sup>

While Schweikert *et al.* suggest that different mass loadings of active material may contribute to differences in impedance,<sup>56</sup> we conclude here that the LTO morphology rather than material loading lies at the origin of the performance variations, since loadings were relatively similar. Impedance performance alone though, does not guarantee high performing material. The two LTO-A samples exhibit reduced resistance upon cycling, but the relatively low average pore size and low specific surface area (Table 2) result in a loss of specific capacity at high C-rates compared to the LTO-B-700, highlighting the intricate interplay of design parameters that must be controlled to optimize LTO performance.

### 3 Conclusions

The goal of this study was the fabrication of mesoporous LTO microspheres as an important next step in LIB materials development. By using block copolymer and homopolymer blends to create templates for sol-gel LTO synthesis, we show that both the molar mass of the BCP, the overall BCP/homopolymer composition, and the annealing temperature yields control over particle size, pore size, crystallite size, and specific surface area of electrode materials. This enables the tunability of key material parameters, allowing the improvement of the electrochemical performance of LTO.

Specifically, a rise in annealing temperature increased the crystallite size and decreased the specific surface area of the LTO material. For instance, the average crystallite size of LTO



annealed at 600 °C was smaller than that of samples annealed at 700 °C (approximately 9 nm *vs.* 11 nm, respectively). This comes, however, at the cost of specific surface area, which was larger for samples annealed at 600 °C compared to those annealed at 700 °C. The mesoporosity of the LTO spheres was controlled through the molar mass of PS in the BCP, maintaining a constant volume fraction ratio of the blocks, yielding pore sizes spanning 5 nm to 20 nm. An anaerobic calcination step caused the carbonisation of the polymer templates, leading to a nanometer-thin carbon layer which provides good electrical conductivity of the resulting LTO material. The optimised balance of these parameters yielded a material with an excellent electrochemical performance, employing BCP-B annealed at 700 °C for 2.5 h, exhibiting a relatively small particle size, and a large specific surface area combined with a large pore size. Apart from high discharge capacities up to C-rates of 30, electrodes made from mesoporous LTO spheres yielded a capacity retention of 95% after 1000 cycles at a C-rate of 10.

The control over detailed morphology demonstrated by this polymer templating method and its resulting effect on LTO electrode performance suggests that even further increases in rate capability and cycle stability may be possible, opening the door to increased LTO utilisation in commercial lithium batteries.

## 4 Experimental

### 4.1 Materials

Polystyrene-*b*-poly(ethylene oxide) (PS-*b*-PEO) block copolymers (BCPs) with a total molar mass of  $M_n = 10\text{-}b\text{-}3.5\text{ kg mol}^{-1}$ ,  $M_n = 18\text{-}b\text{-}7.5\text{ kg mol}^{-1}$ , and  $M_n = 38\text{-}b\text{-}15\text{ kg mol}^{-1}$  were purchased from Polymer Source, Inc. Polystyrene (PS) homopolymer with a total molar mass of 35 kg mol<sup>-1</sup> was purchased from Sigma-Aldrich. Anhydrous tetrahydrofuran (THF, containing 250 ppm butylated hydroxytoluene (BHT) as inhibitor, ≥99.9%), titanium(IV) isopropoxide ( $\text{Ti}[\text{OCH}(\text{CH}_3)_2]_4$ , 97%), 1.0 M lithium ethoxide ( $\text{CH}_3\text{CH}_2\text{OLi}$ ) solution in THF, oxalic acid ( $\text{C}_2\text{H}_2\text{O}_4$ , puriss. p.a., anhydrous, ≥99.0%), and N-methyl-2-pyrrolidone (NMP) (anhydrous, 99.5%) were purchased from Sigma-Aldrich. Conductive carbon black (Super C65) was kindly provided by Imerys Graphite & Carbon, Switzerland Ltd. Polyvinylidene fluoride (PVDF, Kynar) was provided by ARKEMA Innovative Chemistry. Lithium chips were purchased from Gelon LIB Group and GF/B glass microfiber from Healthcare Life Sciences. 1 M lithium hexafluorophosphate ( $\text{LiPF}_6$ ) in 1:1 (v/v) ethylene carbonate (EC):dimethyl carbonate (DMC) was purchased from Solvionic. All chemicals were used as received.

### 4.2 LTO Synthesis

The preparation of mesoporous LTO microspheres was carried out using a three-neck round-bottom flask, which was vacuum-dried overnight at 100 °C before use. During the synthesis, a constant flow of 2.0 mL min<sup>-1</sup> of  $\text{N}_2$  was maintained while the flask was sealed with a rubber stopper and parafilm. Mixing of all precursor solutions was achieved by magnetic stirring.

**Table 4** Chemicals used for the synthesis of mesoporous LTO microspheres

Chemical compounds	Amount (mL)
THF	62
$\text{CH}_3\text{CH}_2\text{OLi}$	1.81
$\text{Ti}[\text{OCH}(\text{CH}_3)_2]_4$	0.65
$\text{C}_2\text{H}_2\text{O}_4$	3.956
PS- <i>b</i> -PEO (BCP)	2.019
PS (HP)	10.1

Prior to the synthesis, a 5.6% (w/w) stock solutions of the PS-*b*-PEO BCPs, PS HP, and oxalic acid in anhydrous THF were prepared. The quantities of all employed chemicals are listed in Table 4.

The LTO synthesis consisted of six steps.

(i) Under constant magnetic stirring, 62 mL THF were first injected into the flask, followed by adding 1.81 mL lithium ethoxide, before slowly adding 0.65 mL titanium(IV) isopropoxide. This initial solution was stirred for two hours, during which its color changed to bright gold before further chemicals were added

(ii) 3.956 mL of oxalic acid were slowly added to the solution, changing its color first to yellow and then back to bright gold. Note that oxalic acid swells the hydrophilic PEO domains<sup>24</sup>

(iii) 2.019 mL of a 5.6% (w/w) solution of PS-*b*-PEO BCP in THF were slowly added to the precursor solution before adding 10.1 mL of a 5.6% (w/w) solution of PS HP in THF, followed by stirring of the precursor solution for two hours

(iv) to evaporate the solvent, the flask was submerged into an oil bath while the temperature was ramped from 40 to 120 °C over the course of two days

(v) the precipitate was vacuum-dried at 100 °C overnight to inhibit water uptake

(vi) to form the spinel  $\text{Li}_4\text{Ti}_5\text{O}_{12}$  structure, the dried precipitate was calcined at 600 °C or 700 °C (Table 1) in a tube furnace under a constant argon flow of 5 L min<sup>-1</sup>. This calcination also burns off the organic compounds and partially converts the polymers into a carbon coating.<sup>21</sup>

### 4.3 Materials characterisation

X-Ray diffraction (XRD) was performed on a Rigaku Ultima IV equipped with a copper target. Fourier-transform infrared spectroscopy (FTIR) spectra were recorded on a PerkinElmer Spectrum 65 spectrometer between 4000 and 450 cm<sup>-1</sup> with a resolution of 8 cm<sup>-1</sup>, averaging 5 scans per sample. Raman spectroscopy was carried out at room temperature on a custom-built setup using an excitation wavelength of 633 nm at a power of 60 mW (LuxX633, Omicron), and acquisition times of 0.5 s. Scanning electron microscope (SEM) images were acquired on a Tescan Mira 3 LMH scanning electron microscope at accelerating voltages of 10 to 20 kV. Thermogravimetric analysis (TGA) was performed on a Mettler Toledo TGA/DSC 1 instrument in a temperature range of 25 to 600 °C with a heating rate of 10 °C min<sup>-1</sup> under  $\text{N}_2$  flow of 30 mL min<sup>-1</sup>. The specific surface area and the pore size distribution of the samples were determined with a Micromeritics Gemini V surface area and pore size analyzer.



#### 4.4 Electrochemical properties of mesoporous LTO microspheres

To characterise the electrochemical performance of the synthesized mesoporous LTO microspheres, composite electrodes were prepared by mixing the LTO particles with carbon black, and poly(vinylidene fluoride) (PVDF) at a ratio of 8:1:1 using aluminum foil as current collector. A homogeneous slurry was created by mixing all powders using pestle and mortar before adding NMP as a solvent. The slurry was cast onto aluminum foil and subsequently doctor-bladed into a 100  $\mu\text{m}$  thick electrode film, and then dried under a fume hood for two days. The dried electrode film was cut into 7/16 inch diameter discs, vacuum-dried overnight at 100  $^{\circ}\text{C}$ , and then transferred into an argon-filled glovebox for assembly into Swagelok cells. A 1/2 inch diameter lithium metal chip was used as the counter electrode and a Grade GF/B Glass microfiber filter was used as separator. Galvanostatic charge-discharge tests were conducted using an Arbin BT 2043 multiple channel cell test system in a voltage range of 1.0 to 2.5 V (vs.  $\text{Li}^+/\text{Li}$ ). Cyclic voltammetry (CV) and electrochemical impedance spectroscopy (EIS) were performed with a BioLogic VMP 300 test system. CV was recorded in a voltage range of 1.0 to 2.5 V (vs.  $\text{Li}^+/\text{Li}$ ), at scan rates of 0.1, 0.2, 0.5, 1.0, and 2.0  $\text{mV s}^{-1}$ . EIS was measured in a frequency range of 1 MHz to 100 mHz with a voltage amplitude of 20 mV. CV was performed at different stages: post-assembly, post-rate test (in order of the following C-rates: 0.5, 1, 2, 5, 10, 20, 30, back to 1; 10 cycles at each C-rate) and post-cycle test (C-rate of 10 for 1000 cycles). While, EIS was conducted post-assembly and post-cycle test.

#### Author contributions

MTN carried out the experiments, PS supervised EIS and CV analysis and discussion, AP discussed material characterization and electrochemical analysis, MGF provided preliminary data, XH, MGF, IG, and US designed the experimental study, IG and US supervised the project. MTN, PS, IG, and US wrote and edited the manuscript.

#### Conflicts of interest

There are no conflicts to declare.

#### Acknowledgements

We thank Dr Dimitri Vanhecke and Dr Bodo D. Wilts for help interpreting the SEM and Raman data. Access to XRD was kindly provided by the Department of Geosciences, University of Fribourg. The authors gratefully acknowledge the financial support from the Swiss National Science Foundation (SNSF). P. S. has been funded by the SNSF under project number P2FRP2-191846. U. S. has been funded by the SNSF through the NRP70 program, Grant 153764. U. S., I. G., and M. T. N. have been funded by the National Center of Competence in Research (NCCR) Bio-Inspired Materials Grant 51NF40-182881. We acknowledge the support of the Adolphe Merkle Foundation.

#### Notes and references

- 1 G. Zubi, R. Dufo-Lopez, M. Carvalho and G. Pasaoglu, *Renewable Sustainable Energy Rev.*, 2018, **89**, 292–308.
- 2 M. Li, J. Lu, Z. Chen and K. Amine, *Adv. Mater.*, 2018, **30**, 1800561.
- 3 M. V. Reddy, G. V. Subba Rao and B. V. R. Chowdari, *Chem. Rev.*, 2013, **113**, 5364–5457.
- 4 Y. Ding, Z. P. Cano, A. Yu, J. Lu and Z. Chen, *Electrochem. Energy Rev.*, 2019, **2**, 1–28.
- 5 G.-N. Zhu, Y.-G. Wang and Y.-Y. Xia, *Energy Environ. Sci.*, 2012, **5**, 6652–6667.
- 6 Z. Chen, H. Li, L. Wu, X. Lu and X. Zhang, *Chem. Rec.*, 2018, **18**, 350–380.
- 7 X. Zeng, M. Li, D. A. El-Hady, W. Alshitari, A. S. Al-Bogami, J. Lu and K. Amine, *Adv. Energy Mater.*, 2019, **9**, 1900161.
- 8 X. Sun, P. V. Radovanovic and B. Cui, *New J. Chem.*, 2014, **39**, 38–63.
- 9 T.-F. Yi, S.-Y. Yang and Y. Xie, *J. Mater. Chem. A*, 2015, **3**, 5750–5777.
- 10 S. Schweißler, L. de Biasi, A. Schiele, P. Hartmann, T. Brezesinski and J. Janek, *J. Phys. Chem. C*, 2018, **122**, 8829–8835.
- 11 T. Yuan, Z. Tan, C. Ma, J. Yang, Z.-F. Ma and S. Zheng, *Adv. Energy Mater.*, 2017, **7**, 1601625.
- 12 B. Zhao, R. Ran, M. Liu and Z. Shao, *Mater. Sci. Eng., R*, 2015, **98**, 1–71.
- 13 G. Yang and S.-J. Park, *J. Mater. Chem. A*, 2020, **8**, 2627–2636.
- 14 J. Liu, A. Wei, G. Pan, S. Shen, Z. Xiao, Y. Zhao and X. Xia, *J. Energy Chem.*, 2021, **54**, 754–760.
- 15 Y. Tang, L. Yang, Z. Qiu and J. Huang, *J. Mater. Chem.*, 2009, **19**, 5980–5984.
- 16 L. Yu, H. B. Wu and X. W. D. Lou, *Adv. Mater.*, 2013, **25**, 2296–2300.
- 17 L. Shen, C. Yuan, H. Luo, X. Zhang, L. Chen and H. Li, *J. Mater. Chem.*, 2011, **21**, 14414–14416.
- 18 C. Lin, X. Fan, Y. Xin, F. Cheng, M. On Lai, H. Zhou and L. Lu, *Nanoscale*, 2014, **6**, 6651–6660.
- 19 M. G. Fischer, X. Hua, B. D. Wilts, I. Gunkel, T. M. Bennett and U. Steiner, *ACS Appl. Mater. Interfaces*, 2017, **9**, 22388–22397.
- 20 E. Kang, Y. S. Jung, G.-H. Kim, J. Chun, U. Wiesner, A. C. Dillon, J. K. Kim and J. Lee, *Adv. Funct. Mater.*, 2011, **21**, 4349–4357.
- 21 M. Christopher Orilall and U. Wiesner, *Chem. Soc. Rev.*, 2011, **40**, 520–535.
- 22 A. Nugroho, K. Y. Chung and J. Kim, *J. Phys. Chem. C*, 2014, **118**, 183–193.
- 23 J. Ma, Y. Wei, L. Gan, C. Wang, H. Xia, W. Lv, J. Li, B. Li, Q.-H. Yang, F. Kang and Y.-B. He, *J. Mater. Chem. A*, 2019, **7**, 1168–1176.
- 24 M. Stefk, J. Song, H. Sai, S. Guldin, P. Boldrighini, M. Christopher Orilall, U. Steiner, S. M. Gruner and U. Wiesner, *J. Mater. Chem. A*, 2015, **3**, 11478–11492.
- 25 G. J. d. A. A. Soler-Illia, A. Louis and C. Sanchez, *Chem. Mater.*, 2002, **14**, 750–759.
- 26 A. L. Patterson, *Phys. Rev.*, 1939, **56**, 978–982.



27 L. Aldon, P. Kubiak, M. Womes, J. C. Jumas, J. Olivier-Fourcade, J. L. Tirado, J. I. Corredor and C. Perez, Vicente, *Chem. Mater.*, 2004, **16**, 5721–5725.

28 C. M. Julien, M. Massot and K. Zaghib, *J. Power Sources*, 2004, **136**, 72–79.

29 I. A. Leonidov, O. N. Leonidova, L. A. Perelyaeva, R. F. Samigullina, S. A. Kovayazina and M. V. Patrakeev, *Phys. Solid State*, 2003, **45**, 2183–2188.

30 X. Li, H.-C. Lin, W.-J. Cui, Q. Xiao and J.-B. Zhao, *ACS Appl. Mater. Interfaces*, 2014, **6**, 7895–7901.

31 K. Mukai, Y. Kato and H. Nakano, *J. Phys. Chem. C*, 2014, **118**, 2992–2999.

32 T. Yuan, X. Yu, R. Cai, Y. Zhou and Z. Shao, *J. Power Sources*, 2010, **195**, 4997–5004.

33 A. Dillon, M. Yudasaka and M. Dresselhaus, *J. Nanosci. Nanotechnol.*, 2004, **4**, 691–703.

34 Y. Xu, X. Chen, L. Wang, K. Bei, J. Wang, I.-M. Chou and Z. Pan, *J. Raman Spectrosc.*, 2020, **51**, 1874–1884.

35 Y. Gao, Z. Wang and L. Chen, *J. Power Sources*, 2014, **245**, 684–690.

36 M. Kruk and M. Jaroniec, *Chem. Mater.*, 2001, **13**, 3169–3183.

37 P. A. Monson, *Microporous Mesoporous Mater.*, 2012, **160**, 47–66.

38 Q. Wang, H. Wang, Y. Wu, L. Cheng, L. Zhu, J. Zhu, Z. Li and Y. Ke, *J. Sol-Gel Sci. Technol.*, 2020, **94**, 186–194.

39 E. Pohjalainen, T. Rauhala, M. Valkeapaa, J. Kallioinen and T. Kallio, *J. Phys. Chem. C*, 2015, **119**, 2277–2283.

40 M. Wagemaker and F. M. Mulder, *Acc. Chem. Res.*, 2013, **46**, 1206–1215.

41 W. J. H. Borghols, M. Wagemaker, U. Lafont, E. M. Kelder and F. M. Mulder, *J. Am. Chem. Soc.*, 2009, **131**, 17786–17792.

42 X. Zhang, C. Lu, H. Peng, X. Wang, Y. Zhang, Z. Wang, Y. Zhong and G. Wang, *Electrochim. Acta*, 2017, **246**, 1237–1247.

43 B. Kurc, *Ionics*, 2018, **24**, 121–131.

44 J. Yue, C. Suchomski, T. Brezesinski and B. M. Smarsly, *ChemNanoMat*, 2015, **1**, 415–421.

45 S. Ganapathy and M. Wagemaker, *ACS Nano*, 2012, **6**, 8702–8712.

46 A. Van der Ven and M. Wagemaker, *Electrochem. Commun.*, 2009, **11**, 881–884.

47 Y. Zhang, Y. Luo, Y. Chen, T. Lu, L. Yan, X. Cui and J. Xie, *ACS Appl. Mater. Interfaces*, 2017, **9**, 17145–17154.

48 H. Utsunomiya, T. Nakajima, Y. Ohzawa, Z. Mazej, B. Zemva and M. Endo, *J. Power Sources*, 2010, **195**, 6805–6810.

49 J. M. Feckl, K. Fominykh, M. Doblinger, D. Fattakhova-Rohlfing and T. Bein, *Angew. Chem., Int. Ed.*, 2012, **51**, 7459–7463.

50 L. Kavan, J. Prochazka, T. M. Spitzer, M. Kalbac, M. Zukalova, T. Drezen and M. Gratzel, *J. Electrochem. Soc.*, 2003, **150**, A1000.

51 J. Rikarte, B. Acebedo, A. Vilalta-Clemente, F. Bonilla, A. J. Wilkinson, M. Galceran, A. Lousa, J. Rubio-Zuazo and M. A. Munoz-Marquez, *Adv. Mater. Interfaces*, 2020, **7**, 1902164.

52 M. Kitta, T. Akita, Y. Maeda and M. Kohyama, *Langmuir*, 2012, **28**, 12384–12392.

53 D. Shao, J. He, Y. Luo, W. Liu, X. Yu and Y. Fang, *J. Solid State Electrochem.*, 2012, **16**, 2047–2053.

54 S. Hao, X. Xiao, Z. Hu, L. Sun, S. Han, D. Chen and X. Liu, *J. Phys. Chem. C*, 2013, **117**, 26889–26895.

55 N. Elgrishi, K. J. Rountree, B. D. McCarthy, E. S. Rountree, T. T. Eisenhart and J. L. Dempsey, *J. Chem. Educ.*, 2018, **95**, 197–206.

56 N. Schweikert, H. Hahn and S. Indris, *Phys. Chem. Chem. Phys.*, 2011, **13**, 6234–6240.

57 N. Schweikert, R. Heinzmann, A. Eichhofer, H. Hahn and S. Indris, *Solid State Ionics*, 2012, **226**, 15–23.

